Ultrasonics 94 (2019) 92–101

Contents lists available at ScienceDirect

Ultrasonics

journal homepage: www.elsevier.com/locate/ultras

The impact of area on BAW resonator performance and an approach to device miniaturization

Ngoc Nguyen[a], Agne Johannessen[a], Stig Rooth[b], Ulrik Hanke[a,*]

[a] Department of Microsystems, University of South-Eastern Norway, Raveien 215, 3184 Borre, Norway
[b] Kongsberg Norspace AS, Knudsrødveien 7, 3189 Horten, Norway

ARTICLE INFO

Keywords:
FBAR
SMR
BAW resonator filters

ABSTRACT

The dependence of the performance of thin film bulk acoustic resonator (FBAR) and solidly mounted resonator (SMR), on their areas is studied with the aid of finite element method (FEM) software. Dual step frame method is applied for both types of the resonators in order to improve their quality factors at resonance and at anti-resonance frequency when they are miniaturized. The important role of the material quality in promoting the benefit of this method is also emphasized in this study.

1. Introduction

The fast growth of mobile handsets worldwide in the past decade has created demanding needs for analog filter modules in terms of high performance and their number per mobile device. The manufacturers keep adding new frequency bands to their next generation smartphones whenever the authorities release the bands. Consequently, the number of analog filter modules per mobile device has recently escalated to 60 and will increase to 100+ due to the evolution of mobile phone technology into 5G [1,2]. This leads to two challenges: overcrowding of physical space and coexistence of many frequency bands a device supports. Filter modules based on bulk acoustic wave (BAW) resonators fulfill the requirements of low cost, high performance, small size and yet good power handling capability [3]. However, placing so many analog filters and multiplexers into a cellphone with limited space for the RF front-end module implies either using tunable filters or enhanced miniaturization of the filter devices, along with a smart packaging strategy. Tunable BAW filters, for which some physical restrictions have to be overcome, were reported to provide limited tuning range of frequency and low quality factors (Q) [4,5]. In addition, the filters must provide high selectivity, i.e. their BAW resonator core elements must have high Q factors, in order to resolve the coexistence challenge in demanding applications. However, this may lead to a sacrifice in the filter bandwidth.

The performance parameters of a BAW resonator are substantially influenced by its area. At resonance frequency f_r of the BAW resonators, due to the high current, ohmic loss dominates, leading to the deterioration of the quality factor Q_r while at antiresonance frequency f_a the acoustic leakage is one of the main loss mechanisms that worsen Q_a [6,7]. As the area of the resonator increases, the electrical current increases hence the effect of ohmic loss is more pronounced. This contributes to the increase of Q_r for smaller resonator areas down to a size were Q_r drops. On the other hand, it is reported that reducing the resonator size leads to the decrease in coupling coefficient and Q_a [8]. Miniaturization of the resonator in order to integrate more analog filters into the RF front-end module, and thus more channels into a given frequency range is meaningless if Q_a degrades too much, i.e. results in too poor steepness of the filter skirt [9]. A method to improve the Q_a for small size resonators is therefore essential. A possible strategy is to reduce the acoustic leakage at f_a using a dual step frame design [10,11] for dual Lamb mode reflection or double-raised borders [12]. In this paper, the dual step frame design is carried out for both types of BAW resonators – thin film bulk acoustic resonator (FBAR) and solidly mounted resonator (SMR). For the SMR, the design procedure also takes into account the reflection of vertically propagating shear waves, apart from the fundamental longitudinal waves, in order to minimize the acoustic loss through the vertical acoustic mirror [13].

FEM simulations are used to study the behavior and evaluate the performance of the BAW designs, including those with no frame, with a single step frame, and with a dual step frame. The active area is varied from 625 μm^2 up to 90,000 μm^2 for the FBAR case. For the SMR case, based on the conclusions from the FBAR results, the area is varied from 3600 μm^2 up to 90,000 μm^2. In order to investigate how material losses influence the usefulness of the dual step frame strategy, simulations with varying material loss parameters are performed. The results show that miniaturization of BAW resonators without degrading Q factors is

* Corresponding author.
E-mail address: ulrik.hanke@usn.no (U. Hanke).

https://doi.org/10.1016/j.ultras.2018.11.014
Received 9 July 2018; Received in revised form 20 November 2018; Accepted 29 November 2018
Available online 14 December 2018
0041-624X/

achievable, given that a proper dual step frame design is applied. Further, the impact of the optimized dual step frame design is higher for lower material acoustic loss factors.

2. FBAR

2.1. Analysis of thickness-extensional (TE_1) resonance for a 1D FBAR with finite electrode area

Standard models used to estimate FBAR performance, like the 1D Mason model, neglects the influence of the mechanical and electrical boundary conditions along the electrode perimeter for finite electrode dimensions. It is shown in [14] that for thin piezoelectric plates the boundary conditions reduce to the continuity of vertical displacements and their derivatives. By this simplification an approximate analytical expression for the admittance Y of the TE_1 trapped energy resonance of the 2D FBAR design with electrode length $2l$ shown in Fig. A.1(b) in the appendix can be found by applying the method proposed in [15].

$$Y(f,l)=\frac{I(f,l)}{V} =\frac{4j\omega l^2\varepsilon_{33}^{f}}{h^f}(\hat{k}^2+1)+\frac{8j\omega l\varepsilon_{33}^{f}\hat{k}^2(G_1^n)^2(\eta_{fn}^0)^2\sin^2(\bar{\xi}_{n\mu}l)}{\left(\frac{\hat{\omega}_{n\mu}^2}{\omega^2}-1\right)G_2^n(h^f)^2(\bar{\xi}_{n\mu})^2L_{n\mu}} \quad (1)$$

Here the current flowing into the FBAR is I and the voltage applied is V. $\omega = 2\pi f$ is the angular frequency and $\hat{\omega}_{n\mu} = 2\pi f_r$ is the angular frequency of the trapped TE_1 mode. Details of derivation and parameter definitions are given in the appendix of this paper. Both resonance frequency f_r of this trapped TE_1 mode, happening when Y is maximum, and antiresonance frequency f_a, occurring when Y is minimum, depend on the electrode area $2l \times 2l$ of the FBAR.

2.2. Modeling and simulation setup

The active region of an FBAR comprises of a piezoelectric layer sandwiched between two metal electrodes. This stratified structure with free top and bottom surfaces makes the FBAR a robust acoustic resonator in terms of energy confinement for the bulk waves traveling in the vertical direction. However, at the periphery of the active region, the resonator suffers from energy loss due to the lateral leakage of propagating Lamb waves. This type of loss has significant contribution at f_a [7], leading to the degradation of the Q_a. In order to diminish the loss, a frame with two steps is added to the perimeter region of the resonator. The performance of this dual-step framed resonator design is compared to those of other FBAR designs as their active areas are varied.

Fig. 1 shows the geometries and the used materials of the 2D FEM models built in COMSOL for three design cases. The first one (Fig. 1(a)) is a conventional FBAR with no frame. The second one (Fig. 1(b)) is an FBAR with a single step frame whose width is three quarter wavelengths of the S_1 mode which is in line with literature [6,16]. This structure provides a high impedance at f_a and thus high Q_a. The third design case, as shown in Fig. 1(c), is an FBAR with a dual step frame designed to be a lateral acoustic mirror that can reflect the two propagating Lamb modes S_1 and A_1. The width of each step is approximately equal to an odd multiple of the quarter wavelength for both S_1 and A_1 modes. The detailed procedure for the design of this frame structure is described in [10]. As indicated in the figure, symmetry is utilized so only half of the resonator geometry is included in the FEM model in order to reduce the simulation time and memory use. All the three resonators have the same area of the active region, i.e. the overlapping area between the top and bottom electrodes. The thicknesses of the layers in the "non-framed" part of the FBAR active regions are chosen so that the resonance frequency is at 2.42 GHz and the antiresonance frequency is at 2.49 GHz for $100 \times 100\ \mu m^2$ area. AlN is chosen as the piezoelectric material because it offers low acoustic loss, high acoustic velocity and the capability for CMOS integration. In order to achieve good electromechanical coupling coefficients for the resonators the thickness ratio of the AlN layer and the electrodes is optimized. The outside regions are terminated with perfectly matched layers (PMLs) in order to avoid the artificially reflected waves from the edges of the structure. Although all the FEM simulation models are 2D, the widths of the active regions are selected to be the same as the lengths $2l$ since this value is required for the calculation of the static capacitance and electrical response. This means that the active regions of all the simulated FBAR designs are squares. The mesh size in the active region for all the models is chosen to be 100 nm, which is smaller than one tenth of the smallest wavelength among the propagating Lamb modes at f_a. The parameters of the materials used in the designs are listed in Table 1. In the simulations, all the materials except AlN are assumed to be isotropic. In the case of AlN – a piezoelectric material that has wurtzite crystalline structure with hexagonal symmetry – the stiffness constants, permittivity and coupling coefficients are obtained from [17].

The ohmic loss due to finite electrode conductivity is included in the simulations by connecting an external series resistor R_s to the resonator via the electrical circuit module in COMSOL. At resonance frequency, this resistor represents the damping of the resonator to which it is connected. The value of R_s approximately equals the DC resistance of the electrodes, i.e. the loss due to eddy currents caused by spurious modes is neglected. Therefore, this value may deviate from the correct value for frequencies below and close to f_r where a relatively large number of strong spurious modes are located. The length l is varied from 12.5 μm to 150 μm in order to examine the effect of area on the overall performance for all the resonator designs depicted in Fig. 1. The

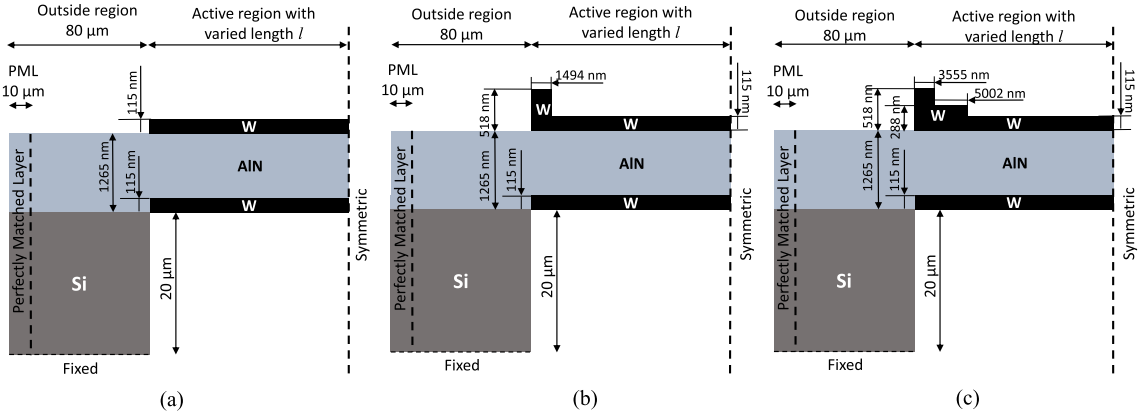

Fig. 1. 2D schematics of the simulated FBARs without frame (a), with a single frame (b), and with a dual step frame (c) designs. The value of l ranges from 12.5 to 150 μm. The resonators are not drawn to scale.

Table 1
Material parameters [18–21].

Parameters	AlN	W	Si	SiO_2	Ir
Density (kg/m^3)	3260	19,350	2181	2200	22,350
Longitudinal wave velocity (m/s)	11,350	5210	8860	6200	5350
Shear wave velocity (m/s)	6090	2880	5310	3950	3240
Resistivity (Ωm)	–	5.6e-8	–	–	4.7e-8
Mechanical loss factor η_s	2.5e-4	5e-4	6e-5	8.4e-4	1.7e-3
Dielectric loss factor	2.0e-3	–	–	–	–

Q factors and effective electromechanical coupling factor k_{eff}^2 are calculated from

$$Q_{r,a} = \pm \frac{f_{r,a}}{2} \frac{d\angle Z}{df}\bigg|_{f=f_{r,a}} \tag{2}$$

$$k_{eff}^2 = \frac{\pi}{2}\frac{f_r}{f_a}\frac{1}{\tan\left(\frac{\pi}{2}\frac{f_r}{f_a}\right)} \tag{3}$$

where Z is the electrical impedance of the resonators.

2.3. 2D FEM simulations

2D simulations are used to study the resonators to reduce computation time and memory use, which are relatively extensive for 3D simulations, especially for the combination of small mesh size and large structures. However, 2D simulations have a limitation that has to be accounted for in order to make reasonable comparisons between the three design cases. Using 2D designs implies that the effect of apodization [6,22] on the resonator performance is not included. Therefore, lateral standing waves caused by Lamb waves, the so-called spurious modes, strongly affect the electrical responses of the resonators. The coupling into spurious modes is even more pronounced as the resonator size shrinks, as reported in previous work [23]. The Q factors calculated based on the 2D FEM simulation results are very sensitive to these modes. If they appear in the proximity of f_a, they can alter the slope of the phase of the electrical impedance, as shown in Fig. 2. This leads to a significant drop in Q_a value independent of resonator active area. This phenomenon occurs in both non-framed and framed FBAR designs. For instance, in the active region of the non-framed FBAR shown in Fig. 1(a), there exists four Lamb modes at f_a – two symmetric modes (S_0, S_1) and two anti-symmetric modes (A_0, A_1). According to Fig. 3, the half wavelengths of the A_0, A_1, S_0, and S_1 modes at f_a are 735 nm,

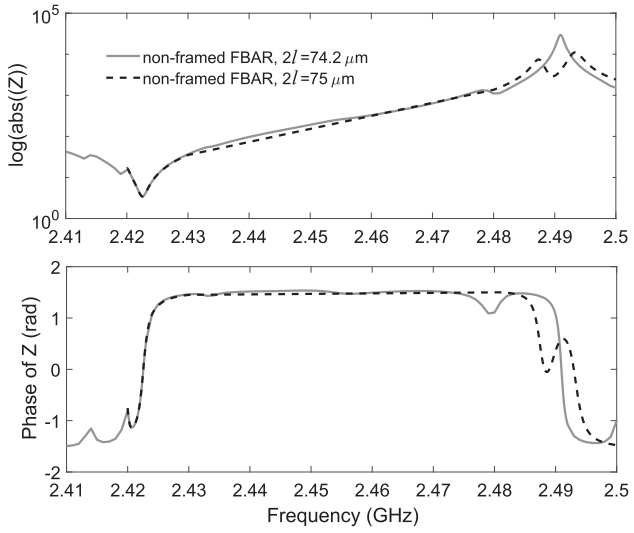

Fig. 2. Electrical responses of the FBAR without a frame for two different areas.

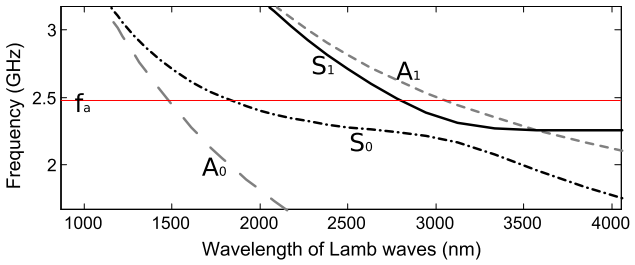

Fig. 3. The wavelength of Lamb waves at f_a in the active region of a non-framed FBAR as in Fig. 1(a) with $2l = 75$ μm.

1512.5 nm, 902.5 nm, and 1387 nm, respectively. It can be readily calculated that the electrode length $2l = 75$ μm is approximately an odd multiple of the S_0 modes half wavelength. It implies that the spurious mode seen in the vicinity of f_a in Fig. 2 (the dashed line) is the lateral resonance of the S_0 mode. Indeed, Fig. 4 shows a repeating pattern of the Q_a variation for the non-framed FBAR as the length l is varied for a short range. The local minima of Q_a occur approximately every 1.8 μm, which is nearly one wavelength λ_{S_0} of the S_0 mode. This result agrees with the condition for the occurrence of lateral standing S_0 waves, namely

$$2l = (2r+1)\frac{\lambda_{S_0}}{2} \tag{4}$$

where r is a non-negative integer. To avoid the sensitivity of the calculated Q factors on the spurious modes, in the following simulations, all the l values of the non-framed FBARs are selected so that the spurious modes do not occur in the vicinity of f_a. However, in the case of the single and dual step framed FBARs, the local minima of Q_a occur in a less predictable way. In order to ensure a fair comparison between the three designs in Fig. 1, a search is done around each evaluated area of the non-framed active region to find the area of the framed design that gives the highest Q_a. This results in a slight difference (about 1–9 μm^2) between the active areas for the three design cases at the same point of evaluation, which, is negligible. It has to be noted that the same phenomenon also happens at resonance frequency as seen in Fig. 2. However, the spurious modes are densely distributed within a frequency range near and below f_r especially when the area of the FBARs increases. Therefore varying l (by very fine steps) is no longer an effective way in avoiding these modes, except when l is really small and the modes are sparsely distributed. The mentioned procedure is thus applied only for avoiding the spurious modes close to f_a.

Simulations are also carried out for two different sets of values of the isotropic mechanical loss factors η_s. The first set is listed in Table 1. For the second set of values, the mechanical loss factor η_s for AlN is changed to 1/6000, i.e. 33% lower than the loss value in the first set. The purpose of these simulations is to compare the impact of the dual step frame design on the resonators' performance for the two different material qualities.

2.4. Results and discussions for the FBARs

Figs. 5–8 respectively show the dependence of the resonance frequency f_r and antiresonance frequency f_a, the electromechanical coupling factor k_{eff}^2, the Q_r factor, and the Q_a factor on the top electrode length, plotted for the three FBAR designs presented in Fig. 1. In Figs. 5 and 6, since the loss factor η_s of AlN does not significantly influence f_r, f_a, and k_{eff}^2, these parameters are plotted only for the set of material loss parameters in Table 1.

In Fig. 5 we see that for all designs, both f_r and f_a reduces from a more or less stable value when top electrode length decreases. The same trend is seen if resonance frequency and antiresonance frequency are calculated from (1) and plotted in Fig. 5 as dotted lines. The analytical formula (1) overestimates the values by about 1% due to the

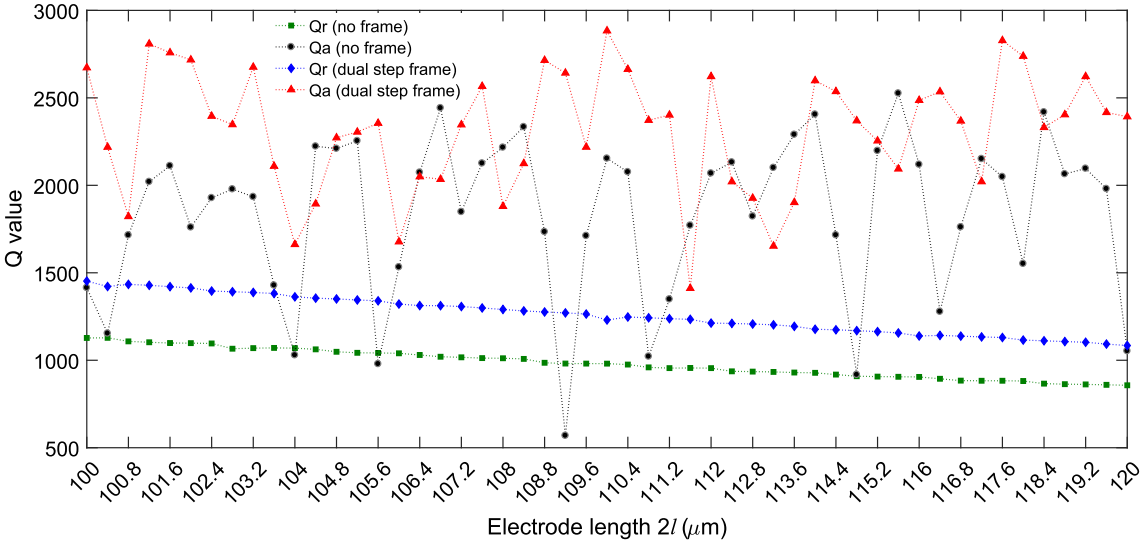

Fig. 4. Q_r and Q_a of the two FBAR designs in Fig. 1(a) and (c) for various lengths $2l$ of the top electrode.

approximate calculation of the vertical propagation component for the active region and the simplified boundary conditions along the electrode edge when the thin plate approximations are applied. However, the decreasing resonance frequency for decreasing electrode length l is predicted. It can be deduced from (A.9) in the appendix that a smaller l results in a larger lateral propagation constant which then combined with (A.13) explains the smaller resonance frequency f_r of the trapped TE_1 mode in the active region compared to the resonance frequency of the pure TE_1 mode. The maximum value of f_r therefore occurs when the active region is significantly larger. Then the lateral Lamb mode propagation constant approaches zero and pure thickness extensional vibration can be assumed. For the FBAR designs with single step and dual step frames, the non–framed active areas reduce, making their f_r smaller than that of the FBAR without frame, especially in the case of the smallest area resonators.

The coupling factor k_{eff}^2 increases with resonator area as shown in Fig. 6 since coupling to undesirable spurious modes coexisting in the resonator is larger for smaller area [24], leading to lower coupling to the main TE_1 mode. In the worst case of FBAR with dual step frame where the active area is $25 \times 25\ \mu m^2$, the resonator provides quite poor coupling. The reason is that part of the energy is shared with the vibration of the frame regions, which have relatively large areas compared to the non-framed active area (≈563 μm² to 62 μm²). These frame steps can be considered as "parasitic resonators" in parallel with the main resonator. They resonate at lower frequencies than the main resonance frequency due to additional electrode mass loading. It means the electromechanical coupling in the dual step framed FBAR is not as high as in the case of a non-framed or a single step frame FBAR. Note that the framed to non-framed active area ratio for the single step frame FBAR is only $140\ \mu m^2/485\ \mu m^2$. This low k_{eff}^2 value leads to a large downward shift of f_a compared to those of the other two FBAR designs of the same size, as shown in Fig. 5(b).

In Fig. 7, Q_r for all designs decreases as l increases, except for the lowest value of l in the case of the dual step framed FBAR. The resonators with relatively small l values are less affected by the ohmic loss, formulated as $R_s|I|^2$, leading to higher Q_r. This is reasonable since the amplitude of the current running through the electrodes, which peaks at f_r, increases with l (and hence Z decreases with resonator area) as described in (A.18) for the non-framed FBAR case. The worst case of the dual step frame FBAR may be due to the dominance of motional loss, occurring when f_r and k_{eff}^2 significantly reduce [25]. For the same area, the dual step frame FBAR design in Fig. 1(c) provides the largest Q_r values due to the reduced resistance in the frame region. This advantage gradually diminishes as l increases. For larger active areas, the current becomes so large that ohmic loss strongly dominates and the contribution of a frame is negligible. In contrast to Q_r, Q_a values for all

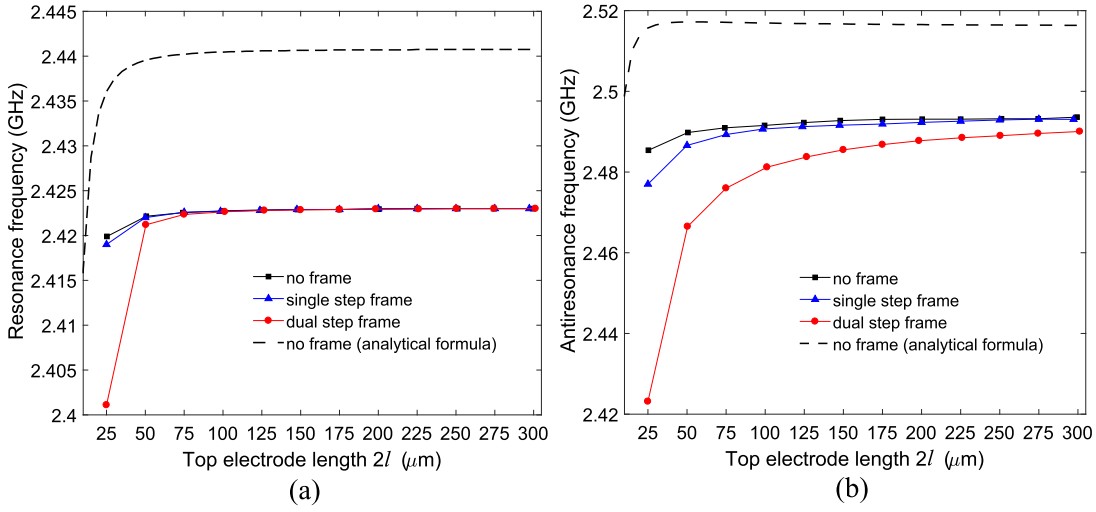

Fig. 5. Resonance (a) and antiresonance (b) frequencies versus top electrode length for the three FBAR designs shown in Fig. 1.

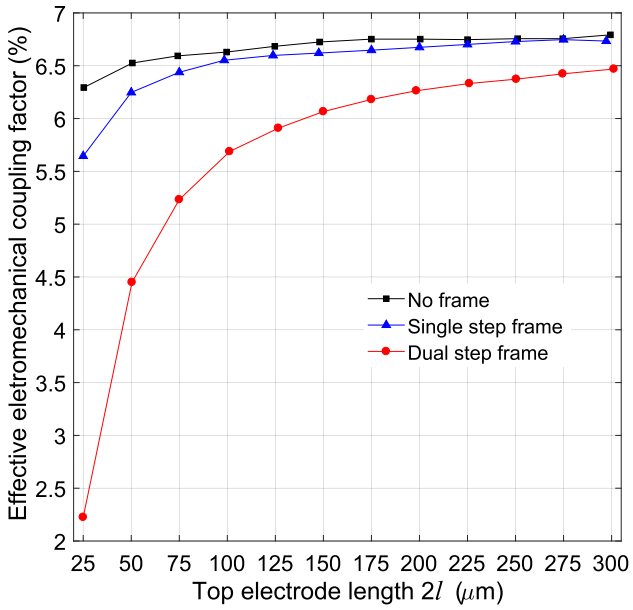

Fig. 6. k_{eff}^2 versus top electrode length plotted for the three FBAR designs presented in Fig. 1.

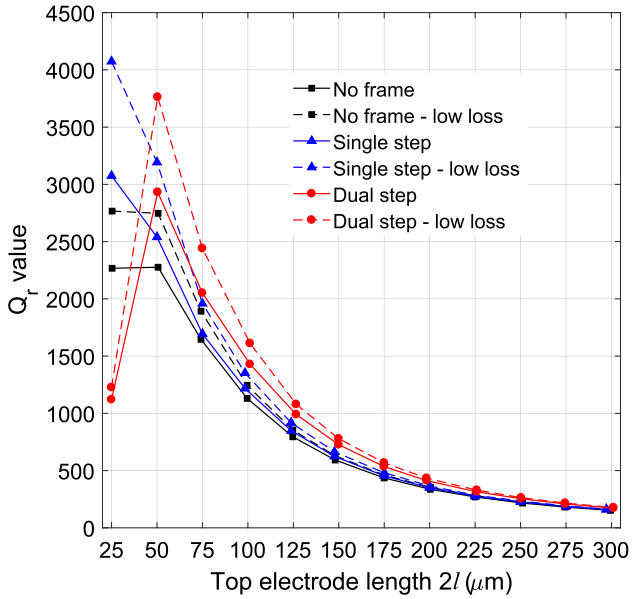

Fig. 7. Q_r of the FBAR designs depicted in Fig. 1 for two sets of material loss parameters: with material loss parameters obtained from Table 1 (solid lines) and with the mechanical loss factor η_s for AlN set to 1/6000 (dashed lines).

three designs tend to increase when l increases as seen in Fig. 8. This can qualitatively be explained by the contribution of the lateral leakage to the total loss in the resonators. The total stored energy of the resonators are proportional to their areas whilst the lateral leakage is proportional to their peripheries. A bigger resonator always has a larger area to periphery ratio, hence larger stored energy to lateral power loss ratio, i.e. larger $Q_a^{lateral}$. The total Q_a is also influenced by other factors, like Q_a^{mech} due to material viscosity and $Q_a^{dielectric}$ due to dielectric loss, which can be expressed as

$$\frac{1}{Q_a} = \frac{1}{Q_a^{lateral}} + \frac{1}{Q_a^{mech}} + \frac{1}{Q_a^{dielectric}} \tag{5}$$

For smaller active area, the lateral leakage is the dominant loss mechanism and Q_a follows $Q_a^{lateral}$. However, when the active area increases, $Q_a^{lateral}$ increases to a point where the other losses start to

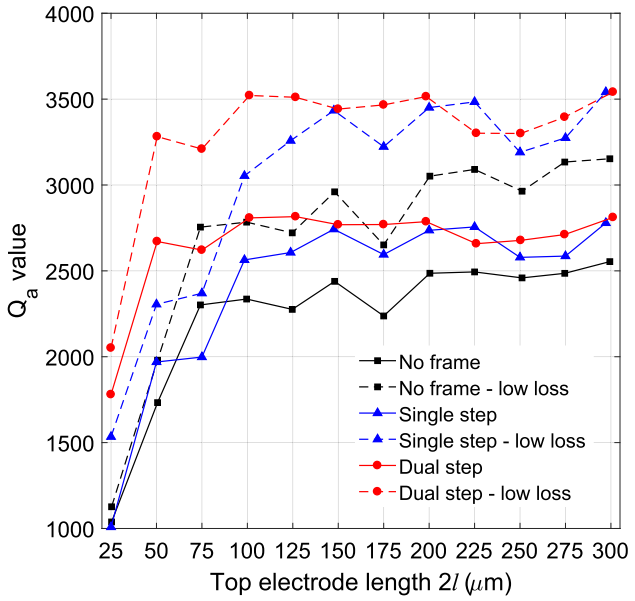

Fig. 8. Q_a of the FBAR designs depicted in Fig. 1 for two sets of material loss parameters: with material loss parameters obtained from Table 1 (solid lines) and with the mechanical loss factor η_s for AlN set to 1/6000 (dashed lines).

dominate and Q_a follows Q_a^{mech} and/or $Q_a^{dielectric}$ which are independent of electrode length $2l$. It means Q_a of each resonator design experiences less drastic change and becomes stable as l continues increasing.

Fig. 8 shows a significant improvement of Q_a that the dual step frame FBAR offers in comparison with the non-framed and the single step frame FBARs, for electrode lengths up to 125 μm. Selecting which design to implement in a filter will then become a trade-off between the coupling factor requirements and the need for high quality factors. For those applications where small resonator area in combination with very high Q are the most critical, the dual step frame design may be the most promising candidate compared to other designs. For wideband applications, if piezoelectric materials with larger intrinsic coupling coefficient, e.g. single crystalline or doped AlN [26,27], the dual step frame FBAR could still be applicable.

Figs. 7 and 8 show that the use of a better quality AlN film can help improve the effectiveness of the dual step frame design in increasing the Q factors of smaller size FBARs. The benefit of high material quality factor on the resonator Q_r, however, diminishes as the resonator area reaches $200 \times 200\ \mu m^2$ due to the dominance of ohmic loss though it is not the case for Q_a.

Fig. 9 compares the total power loss in the outside regions at anti-resonance frequency for the three resonator designs. This loss is calculated from the total acoustic Poynting vector for piezoelectric materials using the FEM simulation software and is normalized to the maximum obtained loss value. In general, the power dissipation to the outside region of the dual step frame FBAR is less than those of the other two designs of the same size. This confirms the benefit of a dual step frame design in alleviating the laterally leaking of acoustic energy.

3. SMR

3.1. Design and modeling

The SMR is a stratified structure consisting of three main parts. The first one, called the resonating part, is a piezoelectric thin film sandwiched between two metal electrodes. The fundamental longitudinal waves (TE_1) are vertically confined in this three-layered stack, forming a standing wave and thus the main resonance. Below this stack is placed an acoustic Bragg mirror that comprises of alternate high and low acoustic impedance layers. The purpose of this mirror is to enhance

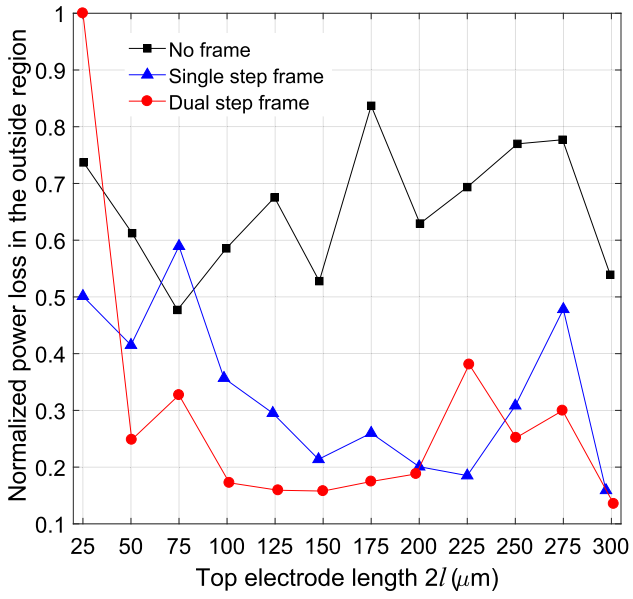

Fig. 9. Normalized power loss to the outside region at f_a, plotted for the various FBAR designs shown in Fig. 1.

reflection of the acoustic waves, so the energy loss into the third part – the substrate below the mirror – is diminished.

In this paper, the SMR is designed to resonate at approximately 2.30 GHz with the antiresonance being at about 2.36 GHz for 100 × 100 μm^2 resonator area. The SMR geometry with thicknesses and materials of all layers is illustrated in Fig. 10(a). All the layers are assumed to be homogeneous and perfectly flat. The mirror of the designed SMR comprises of 4 layers of SiO_2 and 3 layers of Ir alternately stacked together. Ir is chosen for both electrodes and the mirror instead of W as it offers higher acoustic impedance, better conductivity, and better adhesion to the SiO_2 layers in the mirror. The high compressive residual stress in magnetron sputtered W films can cause buckling and delamination [28] in this multilayer structure. In addition, the large ratio between the acoustic impedance of Ir and SiO_2 ensures a good reflectivity for the mirror. In the resonating part of the SMR, although TE_1 is the main mode, thickness shear waves are also excited and if they are not well-confined, they will propagate through the mirror into the substrate significantly degrading the Q factors even if the energy

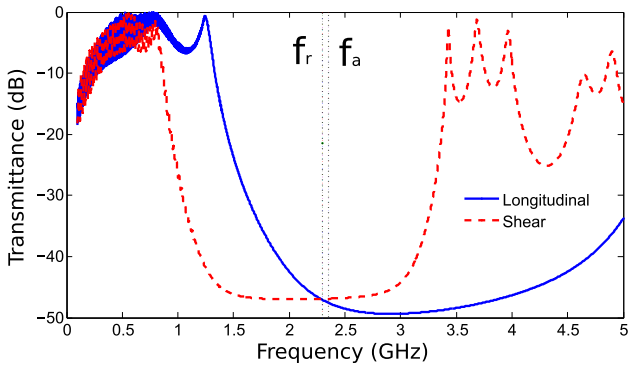

Fig. 11. The transmittance of the mirror that has the SiO_2-Ir configuration shown in Fig. 10.

associated with these waves is small [13]. It is therefore essential to design the mirror that is able to reflect both longitudinal and shear waves at the operating frequencies f_r and f_a. With the mirror configuration shown in Fig. 10 and material properties listed in Table 1, the transmission curves of the two wave modes are plotted in Fig. 11. From the figure, it can be observed that the mirror provides a good reflectivity for both TE_1 and TS_1 modes at f_r and f_a.

For an SMR, the inhibition of acoustic leakage in the lateral direction is as important as for the vertical direction in order to achieve high Q factors, so a dual step frame working as a lateral Bragg mirror is placed at the edge of the active region as in the case of the FBAR. The purpose of this frame is to reflect the two propagating plate modes M_4 and M_5 at f_a as labeled in Fig. 12. This dispersion diagram is obtained by taking the discrete Fourier transform of the vertical displacement component at the surface of the top electrode extracted from FEM simulations. Due to the highly asymmetric semi-infinite SMR structure, Lamb modes can no longer be categorized as symmetric and antisymmetric modes. They are instead called generalized Lamb waves labeled M_i, which have more complicated behavior than the standard Lamb waves [29]. As in the FBAR case, the frame should reflect the two modes that have the largest power, determined by using Poynting's theorem [10]. However, the power analysis for these plate modes are much more complicated in the case of SMR-type BAW resonators and are not carried out in the present paper. Modes M_4 and M_5 are therefore selected since they have the largest velocities among the plate waves and share some similar traits with the two modes S_1 and A_1 in the non-

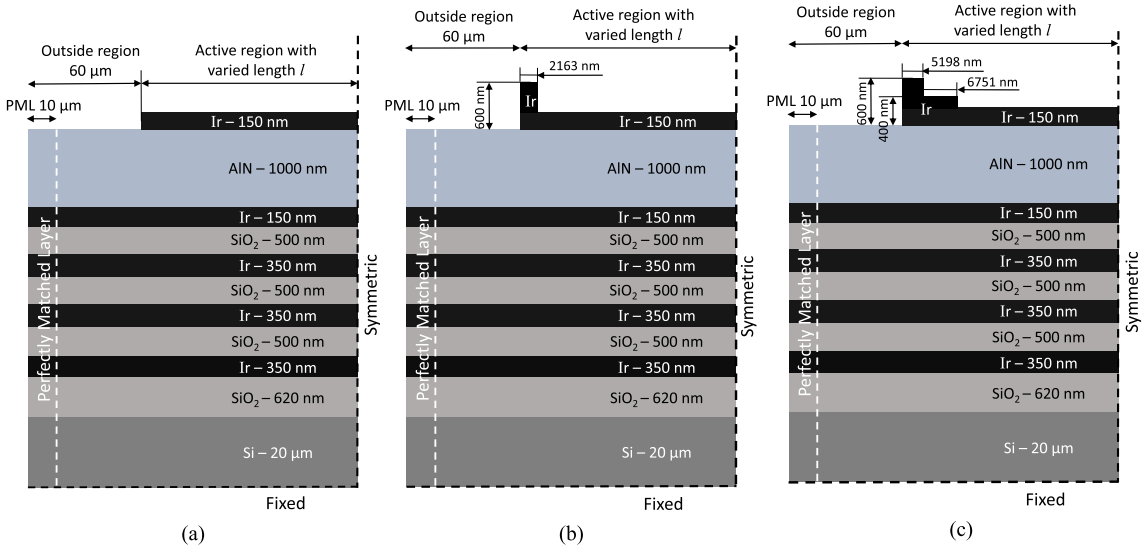

Fig. 10. 2D schematics of the simulated SMR designs without frame (a), with a single frame (b), and with a dual step frame (c). The resonators are not drawn to scale. The value of l ranges from around 30 to 150 μm.

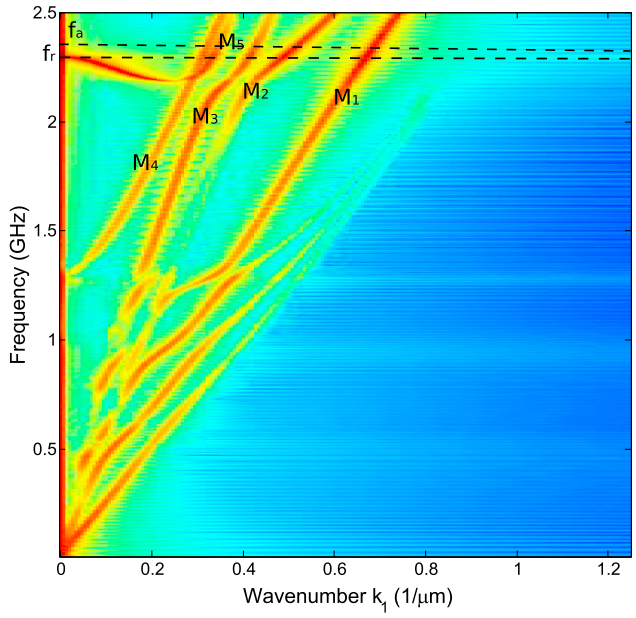

Fig. 12. Dispersion diagram for the active region of the SMR without a frame [Fig. 10(a)].

framed FBAR case. In Fig. 12, the left branch of mode M_5 has negative slope and its cut-off frequency is at the resonance frequency of the trapped TE_1 mode. The mode M_4 has cut-off frequency at the resonance frequency of the trapped thickness shear mode, similar to the A_1 mode.

The frame is designed by finding the wavelengths λ_{M_4} and λ_{M_5} of the M_4 and M_5 modes in the two step regions, and they have to approximately satisfy the equation

$$(2p+1)\frac{\lambda_{M_4}}{4} = (2q+1)\frac{\lambda_{M_5}}{4} \tag{6}$$

where p and q are non-negative integers. As the thickness of the top Ir layer increases, the dispersion of the plate waves changes. The wavelengths of the modes $M_{4,5}$ at f_a are respectively 2439 nm and 3000 nm for the step region of 400 nm high, and are 2344 nm and 2970 nm for the step region of 600 nm high. The resulting (p, q) pairs for the 400 nm-height step is thus (5, 4) and for the 600 nm-height step is (4, 3). The dimensions of the calculated dual step frame SMR is shown in Fig. 10(c). The single step frame SMR design, whose step width equals three quarter wavelength of the mode M_5, as depicted in Fig. 10(b), is also simulated. The area of the active regions does not change when the frame is added. The length l ranges from 30 μm to 150 μm. Smaller values of l are not shown due to the considerably poor coupling factor in the resonators. All the simulated SMRs are square resonators which areas are $2l \times 2l$. As in the FBAR cases, l values are also selected so that the spurious modes occurring near f_a are avoided and the calculated Q_a factors are those least influenced by these modes.

As in the case of FBAR, the influence of material losses on the effectiveness of the dual step frame design is investigated. The simulations for the SMR designs are thus carried out for two different sets of values of the isotropic mechanical loss factors η_s. The first set of values are those obtained from Table 1. For the second set, η_s of AlN, SiO_2, and Ir are set to 1/6000, 1/2000, and 1/1000 respectively. It means a reduction of 33%, 41%, and 70% relative to the loss values listed in Table 1.

3.2. Simulation results for the SMRs

Figs. 13 and 14 show Q_r and Q_a of the three SMR designs in Fig. 10 with various sets of loss parameters. As pointed out previously, the Q_r factor of the resonator decreases with size for all designs. For the same

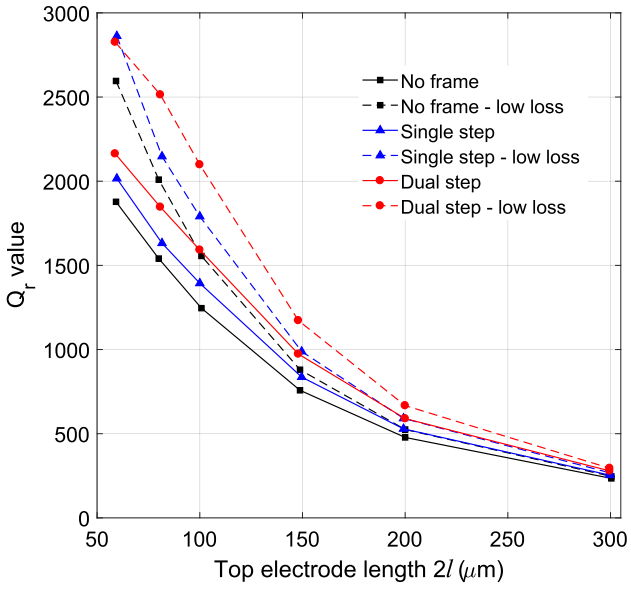

Fig. 13. Q_r of the SMR designs shown in Fig. 10 with material loss parameters obtained from Table 1 (solid lines) and low material losses (dashed lines).

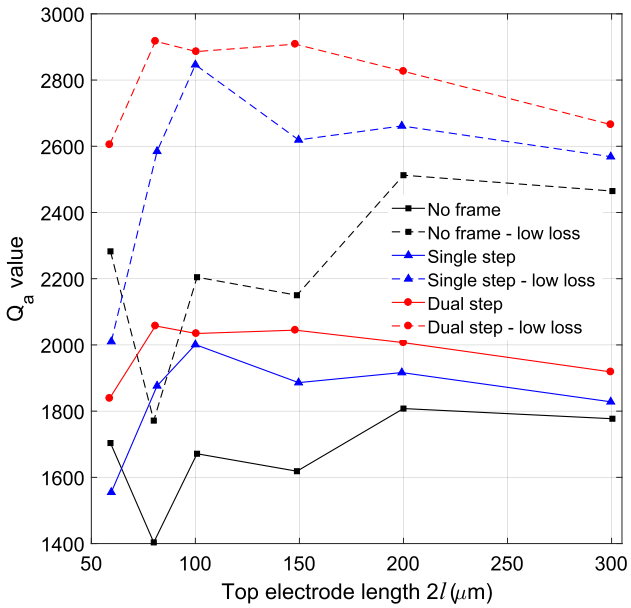

Fig. 14. Q_a of the SMR designs shown in Fig. 10 with material loss parameters obtained from Table 1 (solid lines) and low material losses (dashed lines).

active area, the SMR with a dual step frame design gives marginally higher Q_r due to lower ohmic loss. However, this difference decreases with increasing electrode length. For most of the values of active area, Q_a is higher in the case of dual step frame SMR than for the other two cases.

Compared to a non-framed SMR, an SMR with a dual step frame and with the use of high quality materials offers potentially higher Q factors at both f_r and f_a when its size decreases. More specially, when material losses are reduced, compared to other designs, there is a larger improvement in both Q_r and Q_a of the dual step frame SMR than the improvement obtained with material losses in Table 1. In addition, this improvement is even more pronounced as the resonator area decreases. However, the use of a dual step design comes with the decline of k_{eff}^2 as shown in Fig. 15. This reduction is more distinct than it is for the dual step frame FBAR due to the increased frame area. Since f_r and f_a are not significantly affected by the loss of the used materials, the k_{eff}^2 shown in

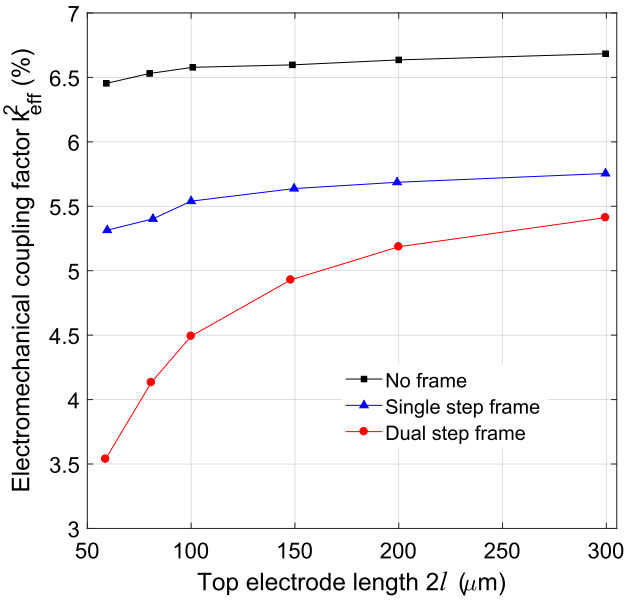

Fig. 15. k^2_{eff} of the three SMR designs depicted in Fig. 10.

Fig. 15 is applicable for both set of material parameters.

4. Conclusions

The area has immense impact on the performance of the BAW resonators. The coupling to spurious modes can be strong at resonance and/or antiresonance frequencies for some specific sizes of resonator areas, causing massive degradation of the Q factors. In designing the BAW resonator, it is thus essentially to avoid these values by using the lateral resonance condition for Lamb modes at the frequencies of interest. The Q_r factor of the resonator increases rapidly as the resonator area is miniaturized. The dual step frame designs significantly improve this Q_r factor compared to those of the non-frame and single step frame resonators of the same size, especially for small area resonators. However, this improvement diminishes as the resonator area increases due to the large influence of ohmic loss on the electrical characteristic. The utilization of the dual step frame, more importantly, helps improve the Q_a factors of the miniaturized non-framed resonators. However, the electromechanical coupling factors of these dual-step-framed resonators reduce as a trade-off. The obtained simulation results also show that the better material quality, the more effective the dual step frame design is in improving the resonator quality factors.

Acknowledgement

This work was supported in part by the University of Oslo and in part by the Norwegian Metacenter for High Performance Computing under Grant NN9344K.

The authors would like to thank Prof. Enrique Iborra and his group at the Technical University of Madrid for providing the software used in designing the acoustic mirror for the simulated SMRs.

Appendix A

Following the approach in [15] in which the structure in Fig. A.1(a) was studied, we analyze the one shown in Fig. A.1(b) with the specified material parameters. Compared to the analyzed structure in [15], in our analysis, a tungsten layer of thickness h^w replaces the silicon layer under the bottom electrode and the bottom electrode thickness h'' is set to zero. This difference does not change the boundary conditions at the layer interfaces and free surfaces in the active or outside regions.

The electrical potential inside AlN and the vertical displacement fields for the trapped thickness-extensional mode n in x_3 direction in the AlN, Si and bottom W layers in the active region when a harmonic bias with amplitude V is applied between the top and bottom electrode are of the forms

$$\bar{u}_3^{fn}(x_1, x_3, t) = (A^n \cos(\eta_n x_3) + B^n \sin(\eta_n x_3)) f^n(x_1, t) + - \frac{e_{33}^f V x_3}{c_{33}^f h^f} e^{j\omega t}, \tag{A.1}$$

$$\bar{\varphi}^{fn}(x_1, x_3, t) = \frac{e_{33}^f}{\varepsilon_{33}^f}(A^n \cos(\eta_n x_3) + B^n \sin(\eta_n x_3)) f^n(x_1, t) + + \left(C x_3 + K + \frac{V x_3}{h^f}\right) e^{j\omega t}. \tag{A.2}$$

The x_3 dependency is governed by pure standing thickness-extensional waves and the constants A^n, B^n, and the propagation constant η_n for each layer can be determined by applying the boundary conditions of zero stress at the surfaces and continuity of fields at the interfaces. The constants C and K are determined by the electrical boundary conditions at the top and bottom electrodes. The vertical displacement field in the AlN layer in the outside region has the same form but with bias V set to zero. For the Si film, the second term in (A.1) and the potential field in (A.2) both vanish.

In the active region the propagation constant $\eta_n = \bar{\eta}_{nf}$ inside the AlN film in the vertical x_3 direction is found by solving

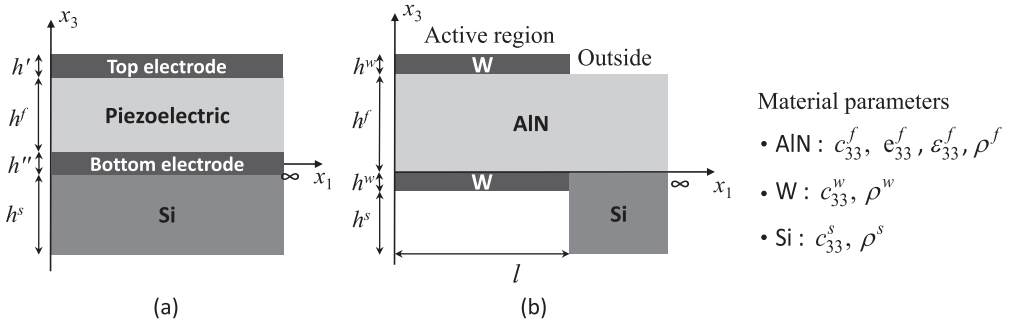

Fig. A.1. The analyzed structure used in [15] (a) and half of the analyzed FBAR structure (b).

$$-2+\frac{\eta}{k^2}\sin\eta+2\cos\eta+2\frac{c^r\mu\eta}{k^2}\cos\eta\tan(\mu\sigma\eta)-c^r\mu\tan(\mu\sigma\eta)\sin\eta+ \\ +R'\left[\frac{\eta^2}{k^2}\cos\eta-\eta\sin\eta-\frac{\eta}{k^2}c^r\mu\eta\sin\eta\tan(\mu\sigma\eta)\right]=0 \tag{A.3}$$

in which $\eta=\bar{\eta}_{nf}h^f$, $k^2=(e_{33}^f)^2/(\bar{c}_{33}^f\varepsilon_{33}^f)=\hat{k}^2/(\hat{k}^2+1)$, $c^r=c_{33}^{\mathrm{w}}/\bar{c}_{33}^f$, $\bar{c}_{33}^f=c_{33}^f+(e_{33}^f)^2/\varepsilon_{33}^f$, $\mu=\sqrt{(\bar{c}_{33}^f\rho^{\mathrm{w}})/c_{33}^{\mathrm{w}}\rho^f}$, $R'=\rho^{\mathrm{w}}h^{\mathrm{w}}/\rho^fh^f$ and $\sigma=h^{\mathrm{w}}/h^f$. All the quantities denoted with a bar on top indicates that these quantities are calculated for the active region except for $\bar{c}_{33}^f$. Further, the resonance frequency for the n^{th} pure thickness-extensional wave is then found from

$$\bar{\omega}_e=\sqrt{\frac{\bar{c}_{33}^f}{\rho^f}}\bar{\eta}_{nf}. \tag{A.4}$$

Similarly, in the outside region, the propagation constant $\eta_n=\eta_{out,n}$ inside the AlN film in the vertical x_3 direction is calculated from

$$\tan(\eta_{out,n}h^f)+c_{out}^r\mu_{out}\tan(\mu_{out}\sigma_{out}\eta_{out,n}h^f)=0 \tag{A.5}$$

where $c_{out}^r=c_{33}^s/\bar{c}_{33}^f$, $\mu_{out}=\sqrt{(\bar{c}_{33}^f\rho^s)/c_{33}^s\rho^f}$, and $\sigma_{out}=h^s/h^f$. The resonance frequency for the pure thickness-extensional wave in the outside region is found from

$$\omega_e^{out}=\sqrt{\frac{\bar{c}_{33}^f}{\rho^f}}\eta_{out,n}. \tag{A.6}$$

The mode shape function in the active region $f^n(x_1,t)$ can be shown to fulfill the inhomogeneous partial differential equation

$$M_n\frac{\partial^2f^n}{\partial x_1^2}-\bar{c}_{33}^f\eta_{fn}^2f^n-\rho^f\frac{\partial^2f^n}{\partial t^2}=\rho^f\omega^2\frac{e_{33}^f}{c_{33}^f}\frac{G_1^n}{h^fG_2^n}Ve^{j\omega t}, \tag{A.7}$$

in which expressions for M_n, G_1^n, and G_2^n can be found in [15]. The mode shape function in the outside region is the solution of a similar partial differential equation with zero bias voltage and material parameters changed accordingly.

We first find solutions of the homogeneous partial differential equation obtained when the bias voltage is set to zero in (A.7). Assuming propagating waves in the active region and a decaying wave on the outside we can write the solutions $f^n(x_1,t)$ to the homogeneous equation for the active and outside regions as

$$f_\mu^n(x_1,t)=\begin{cases}\bar{f}_\mu^n=\bar{E}_n\cos(\bar{\xi}_{n\mu}x_1)e^{i\omega t}, & x_1\leqslant l\\ f_\mu^{out,n}=\bar{E}_n\cos(\bar{\xi}_{n\mu}l)e^{-\xi_{out,n\mu}\left(x_1-l\right)}e^{i\omega t}, & l<x_1<\infty.\end{cases} \tag{A.8}$$

The index μ now refers to the order of the lateral resonance mode. It is shown in [14] that for thin piezoelectric plates the boundary conditions at the border between the active and outside regions reduces to the continuity of vertical displacements and their first order derivatives. This translates to the continuity of $f^n(x_1,t)$ and its first order derivative. Applying these approximate boundary conditions results in the condition for lateral resonance to occur

$$\bar{\xi}_{n\mu}\tan(\bar{\xi}_{n\mu}l)=\xi_{out,n\mu} \tag{A.9}$$

where l is half the electrode length. The dispersion relation for the active region determining the propagation constant $\bar{\xi}_{n\mu}$ in x_1 direction can to the lowest order be written as

$$-\overline{M}_n\bar{\xi}_{n\mu}^2-\bar{c}_{33}^f\bar{\eta}_{nf}^2+\rho^f\omega^2=0 \tag{A.10}$$

in which $\overline{M}_n$ is the value of M_n in the active region. The decay constant $\xi_{out,n\mu}$ is to second order determined from

$$M_{out,n}\xi_{out,n\mu}^2-\bar{c}_{33}^f\eta_{out,n}^2+\rho^f\omega^2=0 \tag{A.11}$$

where $M_{out,n}$ is the value of M_n in the outside region. From (A.10) and (A.11), we have

$$\xi_{out,n\mu}=\sqrt{\frac{\bar{c}_{33}^f}{M_{out,n}}(\eta_{out,n}^2-\bar{\eta}_{nf}^2)-\frac{\overline{M}_n}{M_{out,n}}\bar{\xi}_{n\mu}^2}. \tag{A.12}$$

The lateral resonance frequency of the trapped TE_n mode is now found by substituting solutions of (A.9) into (A.10)

$$\omega_{n\mu}=\sqrt{\frac{1}{\rho^f}(\overline{M}_n\bar{\xi}_{n\mu}^2+\bar{c}_{33}^f\bar{\eta}_{nf}^2)}=\sqrt{\bar{\omega}_e^2+\frac{\overline{M}_n\bar{\xi}_{n\mu}^2}{\rho^f}}. \tag{A.13}$$

Material parameters and layer thicknesses used in this work ensures that the thin plate approximation is valid and that $\xi_{out,n\mu}$ is real and positive. For these layer thicknesses and material parameters $\overline{M}_n$ is negative, so the trapped TE_n mode resonates at a lower frequency than the pure TE_n mode. Now we can use the mode shape functions obtained in the homogeneous case to find solutions of the inhomogeneous Eq. (A.7) by a linear combination of them on the form

$$\bar{f}^n=\sum_\mu H^{n\mu}\bar{f}_\mu^n, \qquad x_1\leqslant l \\ f^{out,n}=\sum_\mu H^{n\mu}f_\mu^{out,n}, \quad l<x_1<\infty \tag{A.14}$$

where $\overline{f}_{\mu}^{n}$ and $f_{\mu}^{out,n}$ take the forms in (A.8). Substituting (A.14) into (A.7) and using (A.13) give

$$\begin{aligned}\sum_{\mu}(\omega^2-\omega_{n\mu}^2)H^{n\mu}\overline{f}_{\mu}^{n} &= \omega^2\frac{e_{33}^{f}}{c_{33}^{f}}\frac{G_1^n}{h^f G_2^n}V, \quad x_1 \leqslant l\\ \sum_{\mu}(\omega^2-\omega_{n\mu}^2)H^{n\mu}f_{\mu}^{out,n} &= 0, \qquad\qquad l < x_1 < \infty.\end{aligned} \tag{A.15}$$

Multiplying with $\overline{f}_{\nu}^{m}$ and $f_{\nu}^{out,m}$ respectively in (A.15) and applying that the mode shape functions to a good approximation are orthogonal leads to

$$H^{n\mu} = \frac{2e_{33}^{f}VG_1^n\sin(\bar{\xi}_{n\mu}l)}{\left(1-\frac{\omega_{n\mu}^2}{\omega^2}\right)c_{33}^{f}G_2^n h^f \bar{\xi}_{n\mu}L_{n\mu}} \tag{A.16}$$

in which

$$L_{n\mu} = 2\left[\int_0^l \overline{f}_{\mu}^{n}\overline{f}_{\mu}^{n}dx_1 + \int_l^{\infty} f_{\mu}^{out,n}f_{\mu}^{out,n}dx_1\right] = l + \frac{\sin(2\bar{\xi}_{n\mu}l)}{2\bar{\xi}_{n\mu}} + \frac{\cos^2(\bar{\xi}_{n\mu}l)}{\xi_{n\mu}^{out}} \tag{A.17}$$

for $n = m$ and $\mu = \nu$. The current through the square top and bottom electrodes is

$$\begin{aligned}I(\omega,l) &= -(2l)2\int_0^l j\omega D_3 dx_1 =\\ &= \frac{4j\omega l^2\varepsilon_{33}^{f}V}{h^f}(\hat{k}^2+1) + \frac{8j\omega lV\varepsilon_{33}^{f}\hat{k}^2(G_1^n)^2(\eta_{fn}^0)^2\sin^2(\bar{\xi}_{n\mu}l)}{\left(\frac{\hat{\omega}_{n\mu}^2}{\omega^2}-1\right)G_2^n(h^f)^2(\bar{\xi}_{n\mu})^2L_{n\mu}}\end{aligned} \tag{A.18}$$

where $D_3 = e_{33}^{f}\bar{u}_{3,3}^{nf} - \varepsilon_{33}^{f}\bar{\varphi}_{,3}^{nf}$, $\hat{\omega}_{n\mu} = \omega_{n\mu} + j\frac{\omega_{n\mu}}{2Q_{unloaded}}$, $Q_{unloaded}$ is the unloaded quality factor, and $\omega_{n\mu} = 2\pi f_{n\mu}$ the lossless resonance frequency of the TE_1–trapped resonator.

References

[1] R. Ruby, A snapshot in time: the future in filters for cell phones, IEEE Microwave Mag. 16 (2015) 46–59.
[2] S. Sethi, FBAR gets excellent reception, Technical Report 11440, The Linley Group, 2015.
[3] P. Warder, A. Link, Golden age for filter design: innovative and proven approaches for acoustic filter, duplexer, and multiplexer design, IEEE Microwave Mag. 16 (2015) 60–72.
[4] K. Hashimoto, T. Kimura, T. Matsumura, H. Hirano, M. Kadota, M. Esashi, S. Tanaka, Moving tunable filters forward: a heterointegration research project for tunable filters combining MEMS and RF SAW/BAW technologies, IEEE Microwave Mag. 16 (2015) 89–97.
[5] R. Aigner, Tunable Filters? reality check foreseeable trends in system architecture for tunable RF filters, IEEE Microwave Mag. 16 (2015) 82–88.
[6] K. Hashimoto (Ed.), RF Bulk Acoustic Wave Filters for Communications, Artech House, 2009, <https://www.thefreelibrary.com/RF+bulk+acoustic+wave+filters+for+communications.-a0207121858>.
[7] R. Thalhammer, R. Aigner, Energy loss mechanisms in SMR-type BAW devices, in: IEEE MTT-S International Microwave Symposium Digest, 2005, 2005, https://doi.org/10.1109/MWSYM.2005.1516565.
[8] C. Muller, M.A. Dubois, Effect of size and shape on the performances of BAW resonators: A model and its applications, in: 2008 IEEE Ultrasonics Symposium, 2008, pp. 1552–1556, https://doi.org/10.1109/ULTSYM.2008.0378.
[9] R. Aigner, S. Marksteiner, L. Elbrecht, W. Nessler, RF-filters in mobile phone applications, in: TRANSDUCERS, Solid-State Sensors, Actuators and Microsystems, 12th International Conference on, 2003, vol. 1, 2003, pp. 891–894, https://doi.org/10.1109/SENSOR.2003.1215618.
[10] N. Nguyen, A. Johannessen, S. Rooth, U. Hanke, A design approach for high-q fbars with a dual-step frame, IEEE Trans. Ultrason. Ferroelectr. Freq. Control 65 (2018) 1717–1725.
[11] N. Nguyen, A. Johannessen, U. Hanke, Design of high-Q Thin Film Bulk Acoustic resonator using dual-mode reflection, in: 2014 IEEE International Ultrasonics Symposium, 2014, pp. 487–490, https://doi.org/10.1109/ULTSYM.2014.0121.
[12] X. Li, J. Bao, Y. Huang, B. Zhang, G. Tang, T. Omori, K.Y. Hashimoto, Use of double-raised-border structure for quality factor enhancement of type II piston mode FBAR, 2017 Joint Conference of the European Frequency and Time Forum and IEEE International Frequency Control Symposium (EFTF/IFCS), 2017, pp. 547–550, , https://doi.org/10.1109/FCS.2017.8088953.
[13] S. Marksteiner, J. Kaitila, G.G. Fattinger, R. Aigner, Optimization of acoustic mirrors for solidly mounted BAW resonators, IEEE Ultrasonics Symposium, 2005. vol. 1, 2005, pp. 329–332, , https://doi.org/10.1109/ULTSYM.2005.1602861.
[14] H. Tiersten, Linear Piezoelectric Plate Vibrations: Elements of the Linear Theory of Piezoelectricity and the Vibrations of Piezoelectric plates, Plenum Press, 1969, <https://books.google.no/books?id=o6QeAQAAIAAJ>.
[15] H.F. Tiersten, D.S. Stevens, An analysis of thickness–extensional trapped energy resonant device structures with rectangular electrodes in the piezoelectric thin film on silicon configuration, J. Appl. Phys. 54 (1983) 5893–5910.
[16] R.K. Thalhammer, J.D. Larson, Finite-element analysis of bulk-acoustic-wave devices: A review of model setup and applications, IEEE Trans. Ultrason. Ferroelectr. Freq. Control 63 (2016) 1624–1635.
[17] J.G. Gualtieri, J.A. Kosinski, A. Ballato, Piezoelectric materials for acoustic wave applications, IEEE Trans. Ultrason. Ferroelectr. Freq. Control 41 (1994) 53–59.
[18] G. Wingqvist, F. Tasndi, A. Zukauskaite, J. Birch, H. Arwin, L. Hultman, Increased electromechanical coupling in w−$Sc_xAl_{1-x}N$, Appl. Phys. Lett. 97 (2010).
[19] P. Muralt, J. Antifakos, M. Cantoni, R. Lanz, F. Martin, Is there a better material for thin film BAW applications than A1n?, in: IEEE Ultrasonics Symposium, 2005., vol. 1, 2005, pp. 315–320, https://doi.org/10.1109/ULTSYM.2005.1602858.
[20] Y. Zhang, D. Chen, Multilayer Integrated Film Bulk Acoustic Resonators, Springer-Verlag, Berlin Heidelberg, 2013.
[21] Private conversations with Enrique Iborra, UPM, Spain, 2016.
[22] R. Ruby, J. Larson, J. Feng, S. Fazzio, The effect of perimeter geometry on FBAR resonator electrical performance, IEEE MTT-S International Microwave Symposium Digest, 2005. 2005, https://doi.org/10.1109/MWSYM.2005.1516563.
[23] T. Pensala, M. Ylilammi, J. Meltaus, K. Kokkonen, P2g-5 Area and dispersion dependence of vibration shape and coupling coefficient in thin film BAW resonators, 2007 IEEE Ultrasonics Symposium Proceedings, 2007, pp. 1661–1664, , https://doi.org/10.1109/ULTSYM.2007.418.
[24] T. Pensala, M. Ylilammi, Spurious resonance suppression in gigahertz-range ZnO thin-film bulk acoustic wave resonators by the boundary frame method: modeling and experiment, IEEE Trans. Ultrason. Ferroelectr. Freq. Control 56 (2009) 1731–1744.
[25] H. Campanella, Acoustic Wave and Electromechanical Resoantors, Artech House, 2010.
[26] J.B. Shealy, J.B. Shealy, P. Patel, M.D. Hodge, R. Vetury, J.R. Shealy, Single crystal aluminum nitride film bulk acoustic resonators, 2016 IEEE Radio and Wireless Symposium (RWS), 2016, pp. 16–19, , https://doi.org/10.1109/RWS.2016.7444351.
[27] T. Yokoyama, Y. Iwazaki, Y. Onda, Y. Sasajima, T. Nishihara, M. Ueda, Highly piezoelectric co-doped AlN thin films for wideband FBAR applications, 2014 IEEE International Ultrasonics Symposium, 2014, pp. 281–288, , https://doi.org/10.1109/ULTSYM.2014.0070.
[28] P. Waters, A.A. Volinsky, Stress and moisture effects on thin film buckling delamination, Exp. Mech. 47 (2007) 163–170.
[29] B.A. Auld, Acoustic waves and fields in solids vol. 2, John Wiley and Sons, New York, 1973.